# FROM REAL WORLD CATALYSIS TO SURFACE SCIENCE AND BACK: CAN NANOSCIENCE HELP TO BRIDGE THE GAP?

H.-J. FREUND, G. RUPPRECHTER, M. BÄUMER, TH. RISSE, N. ERNST, J. LIBUDA
*Fritz-Haber-Institut der Max-Planck-Gesellschaft*
*Faradayweg 4-6, D-14195 Berlin, Germany*

## Abstract

We review the possibilities in using model systems to explore heterogeneous catalytic reactions under ultrahigh-vacuum and in-situ conditions. We discuss metal nano particles deposited on thin oxide films allowing to study hydrogenation and dehydrogenation reactions, while applying a variety of surface sensitive techniques. A second class of systems, where homogeneous catalysts were heterogenized, has been studied under in-situ conditions using ESR spectroscopy.

## 1. Introduction

One prominent example where heterogeneous catalysis affects our daily life is pollution control via exhaust catalysis in everybody's car. Figure 1 shows a schematic diagram with a typical exhaust catalyst in its housing [1]. The catalyst consists of a monolithic backbone covered internally with a wash coat made of mainly alumina but also ceria and zirconia, which itself is mesoporous and holds the small metal particles, often platinum or rhodium. An electron microscope allows us to take a close look at the morphology of the catalyst at the nanometer scale. In order to be active, the metal particles have to be of a few nanometer in diameter and also the support has to be treated in the right way. To a certain extent the preparation is an art, some call it even "black magic". A full understanding of the microscopic processes occurring at the surface of the particles or at the interface between particle and support, however, is unfortunately lacking. We have to realize that catalysis in connection with pollution control – the specific example chosen here - does only utilize a small fraction of the world market for solid catalysts. Human welfare is considerably depending on automotive, petroleum and other industries which constitute a market of $ 100 billion per year and growing rapidly. Given the situation, it is clear that we eventually must achieve a good understanding of the processes. Interestingly, even though the problem is strongly connected to applications, there is a lot of fundamental insight that has to be gained.

*N. Russo et al. (eds.), Metal-Ligand Interactions,* 65–92.

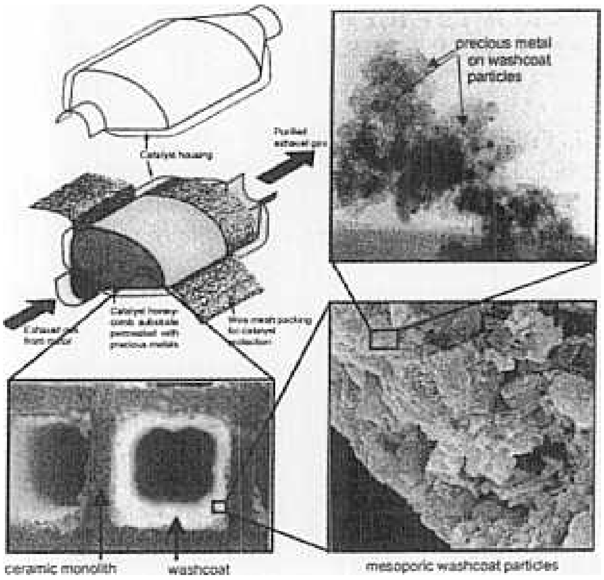

*Figure 1.* Schematic representation of the car exhaust catalyst in its housing. Transmission electron micrographs with increasing resolution show the various constituting ceramic and metallic materials in their morphology. Adapted from [1].

## 1.1. MORPHOLOGY AND STRUCTURE OF MODEL SYSTEMS

Since the complex structure of real catalysts often hampers the attempt to connect macroscopic effects with the microscopic processes taking place on the surface, an increasing number of model studies have been conducted so far to tackle these questions.

Recently, a number of reviews concerning the "surface science approach" have been published taking a critical look at the different strategies to compose and explore model catalysts [2-9]. The spectrum ranges from studies based on polycrystalline or amorphous oxide substrates [2] to investigations on oxide single crystals or well-ordered films [3-9]. Also with respect to the preparation of the particles, different concepts have been proposed. One approach is to apply techniques which come as close as possible to industrial catalyst manufacture like wet impregnation or exchange in solution [2]. Unfortunately, this often involves the disadvantage that structure and morphology of the deposits are rather difficult to control. Thus, vapor deposition of metals [3-9] or deposition of metal clusters from the gas phase [10] under UHV conditions have been preferred in experiments keyed to more fundamental questions about the correlation between structure and properties of small metal particles.

In this context, ultra-thin oxide films grown on a metallic substrate are an excellent choice in order to circumvent problems [3-9] connected with the insulating nature of some bulk oxides. It has been shown that even films with a thickness of just a few Angstroms can exhibit physical properties characteristic of the bulk material [11]. Various groups extensively explored preparation techniques based on the evaporation of a metal (or non-metal) onto a host crystal – mostly a refractory metal – in an ambient oxygen atmosphere [5]. Another promising possibility is the oxidation of a suitable alloy sample containing the metal which should be oxidized. A well-known example of that kind is the formation of well-ordered thin alumina films on the low index surfaces of certain Al alloys [12-18]. But it is not unlikely that this approach also works in other cases [19]. An overview of some well-ordered thin oxide films described in the literature can be found in ref. [20].

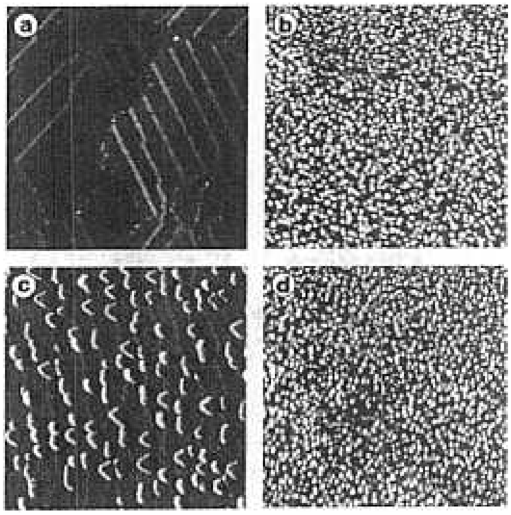

*Figure 2.* Scanning tunneling images (1000 Å × 1000 Å) of *a)* clean alumina film on NiAl(110), *b)* 0.2 Å Pd deposited at 90 K, *c)* 2 Å Pd deposited at 300 K, *d)* 0.2 Å Pd deposited on the pre-hydroxylated film at 300 K.

In Figure 2 we show results on an alumina based model system which has been prepared by oxidation of an NiAl(110) surface and studied via STM in our laboratory [20].

The upper left panel (a) shows the clean alumina surface as imaged by a scanning tunneling microscope [13]. The surface is well ordered and there are several kinds of defects on the surface. One of them are reflection domain boundaries between the two growth directions of $Al_2O_3(0001)$ on the NiAl(110) surface [12]. There are anti-phase domain boundaries within the reflection domains, and, in addition, there are point defects which are not resolved in the images. The morphology does not change dramatically after hydroxylating the film [21, 22]. The additional panels show STM images of palladium deposits on the clean surface at low temperature (b), and at room temperature (c) [20, 23, 24], as well as an image after deposition of Pd at room temperature on a hydroxylated substrate (d) [25]. The amount deposited onto the hydroxylated surface is equivalent to the amount deposited onto the clean alumina surface at room temperature. Upon vapor deposition of Pd at low temperature, small particles (the protrusions shown in Figure 2b) nucleate on the point defects of the substrate and a narrow distribution of sizes of particles is generated. If the deposition of Pd is performed at 300 K, the mobility of Pd atoms is considerably higher so that nucleation at the line defects of the substrate becomes dominant (features line up with the bright lines in Figure 2c). Consequently, all the material nucleates on steps, reflection domain and anti-phase domain boundaries. The particles have a relatively uniform size, in turn depending on the amount of material deposited. If the same amount of material is deposited onto a hydroxylated surface, the particles (the protrusions shown in Figure 2d) are considerably smaller and distributed across the entire surface, i.e. a much higher metal dispersion is obtained which is very similar to the dispersion found at 90 K [21, 26].

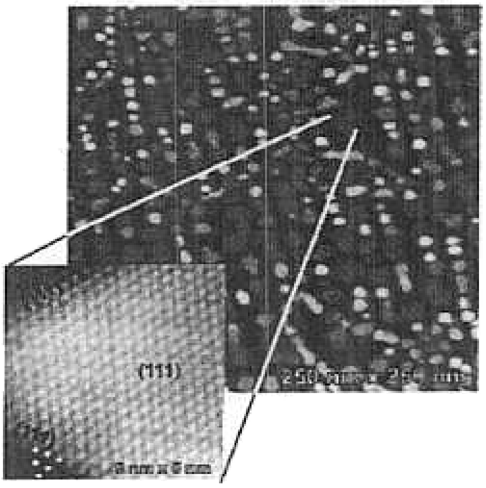

*Figure 3. a)* Scanning tunneling images of a room temperature Pd deposit on $Al_2O_3$/NiAl(110). The inset shows an individual deposit in atomic resolution [27].

The sintering process is an interesting subject. Research on this process is just beginning [20, 26]. A more basic process is metal atom diffusion on oxide substrates. Diffusion studies [28] could profit from atomic resolution, once it is obtained for deposited aggregates on oxide surfaces. While for clean $TiO_2$ surfaces and a few other oxide substrates atomic resolution may be obtained routinely, there are few studies on deposited metal particles where atomic resolution has been reported [29]. A joint effort between Fleming Besenbacher and our group [27] has lead to atomically resolved images of Pd aggregates deposited on the thin alumina film. Figure 3a shows such an image of an aggregate of about 50 Å in width. The particle is crystalline and exposes on its top a (111) facet. Also, on the side, (111) facets, typical for a cuboctahedral particle, can be discerned.

The cluster on the oxide support is schematically represented in Figure 3b. Terrace sites and edge, corner and interface sites are differently shaded in order to make their specificity obvious. These "extra sites" in combination with the finite size of the facets render the situation on a cluster differently from the one encountered on a single-crystal metal surface [30]. We will show further below how specific sizes on these clusters influence the selectivity of a chemical reaction.

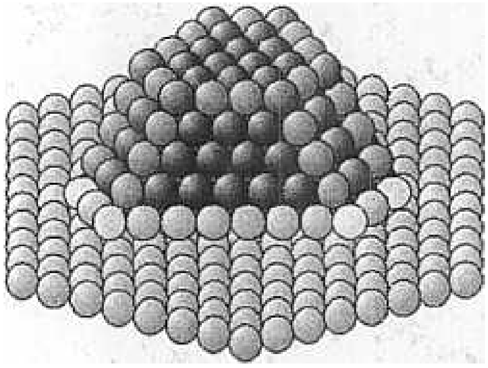

*Figure 3. b)* Schematic representation of a cubooctahedral metal cluster on a substrate.

Before we proceed to reactivity studies we discuss how we can use morphological information to study the preparation of alloyed nanoparticles.

Such materials represent a highly interesting class of catalysts. This is due to the fact that one metal can tune and/or modify the catalytic properties of the other metal as the result of both ligand (electronic) and ensemble (structural) effects [31]. Bimetallic clusters of Pd and Co, for example, have shown improved selectivity over pure Co in Fisher-Tropsch reactions [32-36]. Since the conversion of natural resources into syngas ($CO + H_2$) and then to clean fuels through the Fisher-Tropsch reaction will likely become evermore important with changing supplies and environmental concerns [37], a detailed understanding of such effects by means of suitable model systems is urgently needed. The approach, we have chosen, is based on metal vapour deposition on a suitable oxide support under ultrahigh vacuum conditions. For the present study, the thin alumina film grown on NiAl(110) [12] was used, which enabled us to apply scanning tunneling microscopy as well as thermal desorption spectroscopy for the characterization of the samples. On this film, nanometer-sized Pd-Co particles were generated by *subsequently* depositing the two constituents onto this support. Inspired by earlier work by Henry and coworkers relying on codeposition techniques [38, 39], different structures and compositions were obtained in a controllable way by taking advantage of the different nucleation and growth properties of the two metals.

This is demonstrated in Figure 4 by STM images taken after depositing Pd and Co alone and together on this film. In contrast to Pd (see discussion above), pure Co preferentially nucleates at point defects on the alumina film at 300 K. As can be inferred from the corresponding STM image [40, 41], this results in both a higher particle density and a more homogeneous particle distribution on the surface. Unlike Pd, there are no indications of crystalline order.

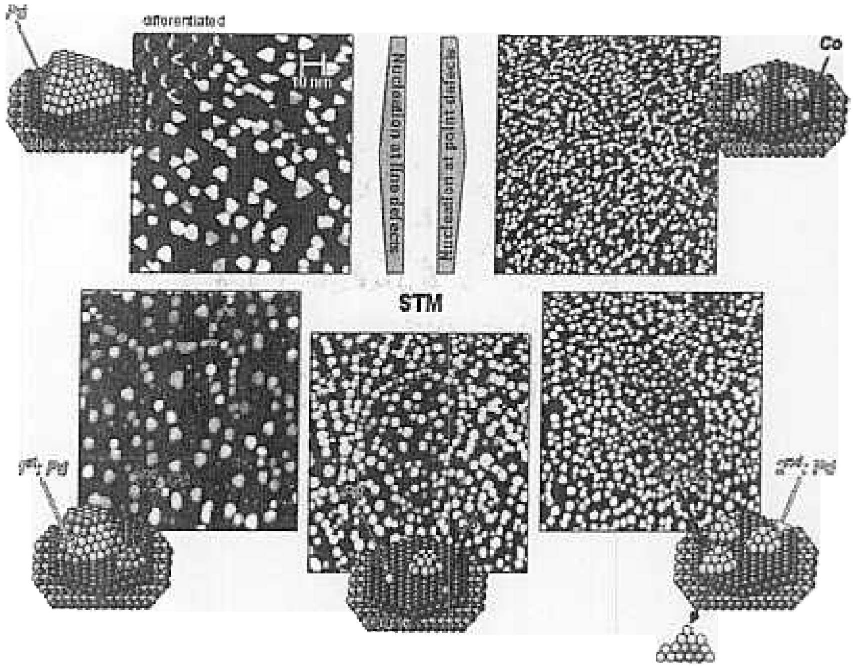

*Figure 4.* 100 nm x 100 nm STM images taken after depositing 2 Å Pd and 2 Å Co alone (top panel) and together (bottom panel) onto a thin alumina film at 300 K. In the latter case the metals have either been deposited subsequently (left: 1st Pd, 2nd Co; right: 1st Co, 2nd Pd) or simultaneously (middle) [42].

Let us now assume that Pd is deposited on a surface already covered by Co particles. Due to the higher mobility of Pd on the surface, it will be trapped at Co particles before reaching the line defects. The STM image presented in Figure 4 essentially corroborates this expectation. The arrangement of particles found for this sequence strongly resembles the situation for pure Co thus suggesting particles with a Co core and a Pd shell. If, on the other hand, Pd is deposited first, the less mobile Co atoms should partly cover the Pd crystallites and partly nucleate between them. The STM image indeed shows triangular crystallites as well as a number of new small clusters in between.

In addition to these sequential deposition experiments, we also performed a codeposition experiment. The corresponding STM image is also included in Figure 4 and reveals a situation intermediate between the results of the stepwise preparation. As the structure of these particles (alloy particles or core/shell structures) is presently unclear, they will not be considered in the following.

In order to verify the surface composition TDS investigations using CO as a probe molecule have been performed [42]. Without going into the details, these studies basically confirm that it is indeed possible to control the formation of alloyed deposited particles by taking advantage of nucleation and growth processes on the surface.

Coming back to the structural properties of the deposited particles we present in the following an example evidencing the importance of specific sites on the particles in steering the selectivity of a chemical reaction.

As a model reaction we choose the decomposition of methanol on the well-ordered Pd crystallites [43]. For this reaction system two competing decomposition pathways exist (see Figure 5): Whereas dehydrogenation to CO represents the dominating reaction channel [44, 45], slow carbon-oxygen bond breakage leads to formation of adsorbed carbon and $CH_x$ species [45-47].

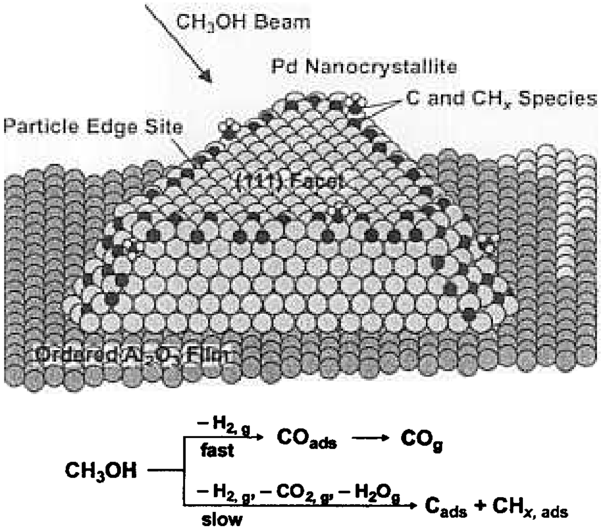

*Figure 5.* Schematic representation of the supported Pd nanoparticles and the blocking of defect sites by carbon species during methanol decomposition

We show that on ordered Pd crystallites these carbon and hydrocarbon species preferentially block defect sites on the particles such as particle edges and steps (see Figure 5). With increasing carbon coverage the rate of carbon-oxygen bond breakage drops rapidly, whereas the kinetics of dehydrogenation is hardly affected. From this, we conclude that activity for carbon-oxygen bond breakage is drastically enhanced at the particle defect sites, whereas this is not the case for the dehydrogenation pathway.

This type of detailed investigations is made possible by two factors:
First, we employ a supported model catalyst, described above.
Secondly, we use molecular beam techniques to study kinetics.

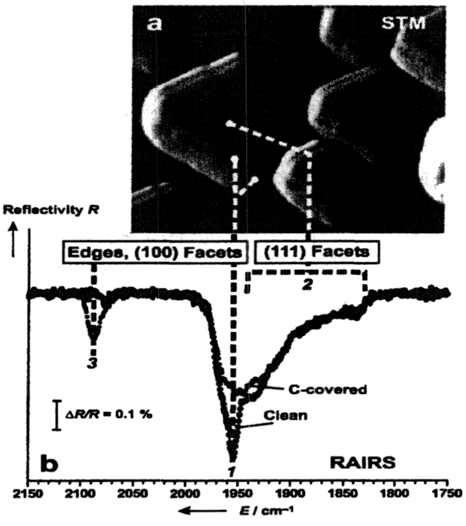

*Figure 6. a)* STM image of the Pd particles grown at 300 K on $Al_2O_3$/NiAl(110) (20 nm × 20 nm), from [48]; *b)* RAIR spectra for CO adsorbed on Pd/$Al_2O_3$/NiAl(110) (sample temperature 100 K, after CO exposure at 300 K). Open symbols: immediately after preparation; solid symbols: after prolonged exposure to methanol at 440 K.

The Pd aggregates represent well shaped crystallites with an average size of approximately 6 nm. They grow in (111) orientation and predominantly expose (111) facets as well as a small fraction of (100) facets. In Figure 6a an STM (scanning tunneling microscopy) image of the particles is shown. Further structural details can be found in the literature [49].

Without going into details, which have been published recently [43], it can be shown that C-O bond cleavage occurs very quickly in the early stages of the reaction, creating carbon atoms which self-poison this oxide reaction favouring methanol dehydrogenation which continues to occur on the facts of the particles. In fact, we find that the ratio between the rates of dehydrogenation and carbon oxygen-bond cleavage $r_{CO}/r_C$ increases from 30 on the pristine sample to approximately 1000 on the carbon contaminated sample.

The question arises where on the nanoparticles the carbon deposits are located. This question is answered by RAIRS using CO as a probe molecule. The corresponding spectra for the pristine Pd particles and after prolonged exposure to methanol are compared in Figure 6b.

For the pristine sample (Figure 6b, open symbols), the spectrum is dominated by a sharp absorption feature at 1960 $cm^{-1}$ (1) with a broad low-frequency shoulder (2) (1930 $cm^{-1}$ to 1840 $cm^{-1}$) and a additional weak feature at 2080 $cm^{-1}$ (3). Previously, the features between 1930 $cm^{-1}$ and 1840 $cm^{-1}$ (2) have been assigned to CO adsorbed on bridge and hollow sites on Pd(111), and the absorption peak at 2080 $cm^{-1}$ (3) to on-top CO on Pd(111) [24, 50]. A detailed comparison with previous work shows that the prominent absorption band at 1960 $cm^{-1}$ (1) originates from a superposition of bridge bonded CO on (100) facets and CO adsorbed at defect sites such as particle edges or steps [24, 50]. The contribution of (100) facets, however, is expected to be small due to the minor fraction of these facets and their tilted geometry (as a consequence of the surface selection rule, IR absorption is attenuated on small tilted facets, e.g. [51]). Following these arguments, we assume that the absorption feature at 1960 $cm^{-1}$ is dominated by CO adsorbed on defect sites, mainly steps and particle edges (see Figure 5). Note, however, that the signals are expected to be strongly modified by dipole coupling effects [52]. As a consequence, the relative intensities do not directly reflect the relative abundance of the corresponding sites, but the defect feature at high frequency is expected to gain intensity at the expense of the regular absorption signal.

After extended exposure to methanol, drastic changes are observed (Figure 6b, solid symbols). The defect peak at 1960 $cm^{-1}$ (1) vanishes almost completely, whereas the absorption signal in the on-top region (3) strongly increases (2090 $cm^{-1}$). All other features in the spectrum, in particular the region below 1950 $cm^{-1}$ (regular facets), remain practically unchanged. Although dipole-coupling effects mentioned above preclude a straightforward quantification, it is apparent from these observations that adsorption at particle defect sites (i.e. steps and edges) is blocked by carbon species formed via carbon-oxygen bond breakage. We conclude that these carbon species preferentially accumulate at defect sites.

In conclusion of this part, we have shown that there is direct evidence for the difference in activity of various reactive sites on a well defined supported metal catalyst steering the selectivity of a reaction.

## 1.2. CONTROLLING THE PARTICLE SIZE FOR REACTIVITY

Another feature of small particle systems is the dependence of a chemical reaction on the size of the deposited particles as alluded to in the introduction. We report here on a study of hydrogenation of ethene in order to investigate the size-reactivity relationship again on Pd nanoparticles. Before turning to the hydrogenation reaction, it is useful first to summarize the adsorption behavior of ethene and hydrogen alone.

Combining the results from a thermal desorption spectroscopy (TDS) and IRAS [24, 53, 54] study, we have proposed a general scheme for ethene thermal transformations on Pd particles, as depicted schematically in Figure 7. On small Pd particles, ethene is mainly $\pi$-bonded at low temperatures and desorbs intact upon heating. On the larger Pd particles, however, a fraction of the ethene molecules is di-$\sigma$ bonded. Again, weakly bonded ethene desorbs intact, (its conversion to di-$\sigma$ species on heating cannot be excluded, however) while di-$\sigma$ ethene can either desorb near room temperature or dehydrogenate producing surface species, such as ethylidyne and atomic hydrogen. Dehydrogenation proceeds further on heating until a hydrogen-deficient carbonaceous deposit and hydrogen are formed at elevated temperatures. Hydrogen atoms recombine and desorb as hydrogen molecules. Finally, the surface remains covered by carbon deposits at elevated temperatures.

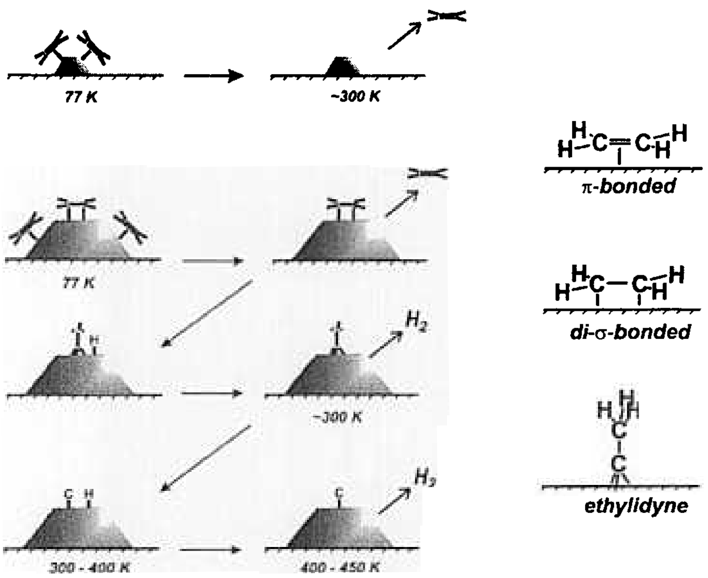

*Figure 7.* Schematic representation of the thermal transformation of ethene on Pd particles of different size.

Accordingly, particle size and roughness strongly influence the distribution of π- and di-σ bonded ethene molecules. Due to the development of more extended facets on the large particles, which favor ethene di-σ bonding, the reaction pathway shifts towards dehydrogenation and hence to the formation of carbon deposits upon heating.

For pure hydrogen adsorption two adsorption states can be distinguished. One state, leading to desorption around 330 K (called $\beta_2$) is very likely due to hydrogen atoms on the surface of the particles while a second one desorbing at lower temperatures ($\beta_1$ at ~ 280 K) is tentatively assigned to subsurface hydrogen. As a function of particle size $\beta_2$ shifts to lower temperature with increasing particle size d, ranging from $1 \text{ nm} < d < 5 \text{ nm}$. The formation of the $\beta_1$ state is decreased on the smallest particles, its desorption temperature being less influenced by the size of the particles. This can be a result of the decreasing number of subsurface sites available or due to the presence of the support.

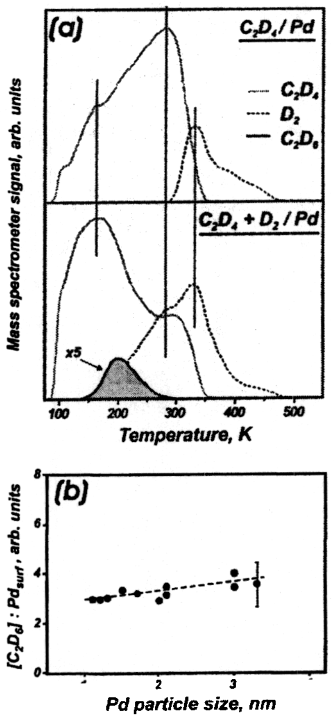

*Figure 8. a)* Thermal desorption spectra of $D_2$, $C_2D_4$ and $C_2D_6$ after exposure of deposited particles of 2 nm average size: top: 1 L of $C_2D_4$ at 90 K bottom: 3 L of $D_2$ at 195 K followed by 1 L of $C_2D_4$ at 90 K, *b)* Integrated signal of ethane (shaded in Fig. 8a) per Pd unit surface area as a function of particle size.

Figure 8 shows TDS spectra obtained after ethene ($C_2D_4$) adsorption with and without hydrogen ($D_2$) preadsorption on clean Pd particles of identical size. We recorded the signals of masses corresponding to $D_2$, $C_2D_4$ and $C_2D_6$. Comparing these spectra, firstly, we observe the formation of ethane, desorbing at ~200 K as the product of ethene hydrogenation. Secondly, the amount of ethene desorbing at temperatures below 200 K is significantly increased, while the intensity of the state at about 280 K is reduced by a factor of 2. Therefore, the data indicate that it is the formation of di-σ ethene that is inhibited by D ad-atoms. This can be understood by assuming that the surface D atoms, residing presumably in the hollow sites, sterically hinder the di-σ-bonding. Meanwhile, ethene can readily adsorb on the D-covered surface via a π-bond on on-top sites. Therefore, hydrogen pre-adsorption leads to a re-distribution of π- and di-σ-bonded ethene, thus favoring a weakly bonded π-state.

In the reverse experiments, when the Pd particles were ethene pre-covered before exposure to $D_2$, the spectra were found to be identical to those when there was no $D_2$ exposure at all. This manifests a site-blocking effect of ethene on hydrogen adsorption.

Such an effect can be readily explained by the fact that hydrogen dissociation occurs on on-top sites (see review in ref. [55]), which are occupied by $\pi$-bonded ethene.

In the absence of pre-adsorbed hydrogen, a very small amount of ethane desorbing at ca. 280 K was detected only for particles larger than 30 Å. This process, called self-hydrogenation, involves the reaction of ethene with hydrogen ad-atoms produced by dehydrogenation of other ethene molecules. Certainly, such a reaction occurs only on the relatively large particles due to an increasing probability of ethene dehydrogenation (see Figure 7). Nevertheless, the amount of ethane produced by self-hydrogenation is negligibly small as compared to that detected in co-adsorption experiments. Moreover, the desorption temperature of ethane formed under co-adsorption conditions is about 80 K lower than in a self-hydrogenation reaction (200 K vs. 280 K). Such a behavior (a temperature shift and an enhanced ethane production) has also been found on hydrogen pre-covered Pt(111) [56] and Pd(110) [57] surfaces. Therefore, it appears that a general mechanism of ethene interaction with hydrogen on metal surfaces is valid on both single crystals and small metal particles.

Our TDS study [53] shows that ethene reacts with the most weakly bonded hydrogen present on the surface. The formation of ethane depends on the presence of weakly adsorbed hydrogen which reacts with $\pi$-bonded ethene before the latter desorbs intact.

In order to study particle size effects, we have carried out experiments for identical preparations varying only the amount of deposited Pd, i.e. particle size.
Figure 8b shows the plot of ethane production per Pd unit surface area as a function of particle size. This plot clearly demonstrates that the hydrogenation activity under the co-adsorption conditions studied is almost independent of the Pd particle size in the 1-3 nm range.

Such a behavior can be understood by the fact that pre-adsorbed hydrogen strongly inhibits the formation of di-$\sigma$-bonded ethene and results in preferential formation of the $\pi$-bonded ethene for all particles sizes studied, thus neutralizing the overall particle size influence observed for pure ethene (see above)

The size independence for ethene hydrogenation obtained in the present work agrees well with the general opinion that this reaction is structure insensitive [58], and it seems that our system represents a suitable model system for studying the mechanism of the reaction, even using UHV conditions.

The influence of carbonaceous deposits on the particle size dependence of the ethene hydrogenation reaction has been studied by creating such deposits via dehydrogenation of ethene before exposing the model catalyst to the reaction mixture [59]. It is shown that carbonaceous deposits do not prevent adsorption but inhibit dehydrogenation of di-$\sigma$-bonded ethene. Using CO as a probe molecule, it can be shown that the carbon deposits occupy highly coordinated sites on the surface. Ethene hydrogenation is inhibited by the presence of carbon deposits but the inhibition is independent of particle size in the range studied (1-3 nm).

Clearly, the results reported for ethene hydrogenation have been obtained under ultrahigh vacuum conditions and the question currently asked is, are the results compatible with results under realistic reaction conditions? We have exposed the same model catalyst as studied above to ambient conditions and measured turnover frequencies (TOF) via gas-chromatography as typically done in a catalytic study [60]. At the same time, we can follow the species on the surface with an in-situ vibrational spectroscopy, namely sum-frequency generation (SFG) that allows us to measure vibrational spectra in the presence of a gas phase. The latter method has been reviewed recently by Rupprechter [61] and applied to nanoparticle model catalysts by Dellwig et al. [62].

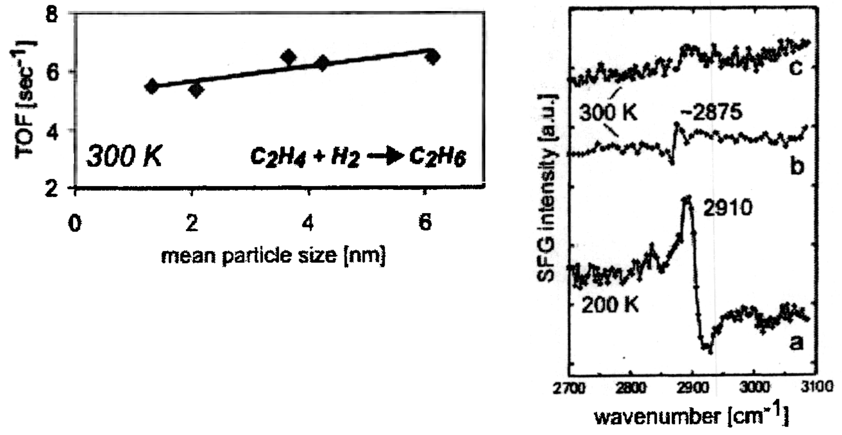

*Figure 9.* Ethene hydrogenation activity of Pd/$Al_2O_3$/NiAl(110) model catalysts with a mean Pd particle size of 1 to 6 nm. The reaction was carried out with 50 mbar $C_2H_4$, 215 mbar $H_2$ and 770 mbar He at 300 K. SFG spectra of $C_2H_4$ on Pd(111) are shown for different conditions: Di-σ bonded ethene was observed after saturation at 200 K *(a)*, while a weak signal of ethylidine appeared upon room temperature exposure of ethene *(b)*. The absence of strong signals under reaction conditions (5 mbar $C_2H_4$, 5 mbar $H_2$) suggests the presence of π-bonded ethene [63].

Figure 9 shows turnover frequencies as a function of particle size measured on model catalysts prepared in the same way as used for the ultrahigh vacuum studies [59, 60]. The model catalyst was placed in a reaction vessel [64] and exposed to a mixture of $C_2H_4$ (50 mbar), $H_2$ (215 mbar) and He (770 mbar) with ethane production being monitored by on-line gas chromatography at various temperatures and reaction times [60]. Knowing the structure and morphology of the catalyst, turnover frequencies are calculated. The system turned out to be stable under reaction. The TOFs are rather independent of particle size and the activation energy for ethene hydrogenation from temperature dependent data amounts ca. 55 kJ/mol [60]. There is a remarkable correspondence of particle size dependent properties under ultrahigh vacuum and ambient conditions which already at this stage can be taken as indication that the mechanisms are similar under both conditions. SFG spectroscopy can be applied as an in-situ technique during reactions and spectra on Pd(111) as a model surface are also shown in Figure 9 [63]. To identify the species involved, UHV adsorption studies were initially performed. At 200 K (Figure 9, trace a), a characteristic spectrum of di-σ-bonded ethene was observed, while π-bonded ethene shows no signal due to its parallel geometry on the (111) surface (with C-H bonds still being in plane). At 300 K, a small signal from ethylidyne appeared due to ethene decomposition (trace b). Under reaction conditions (Figure 9, trace c) no distinct signals are observed suggesting that both di-σ-bonded ethene and ethylidyne are not turning over and that rather π-bonded ethene is the active species. The SFG spectra provide considerable indirect evidence for this conclusion. Experiments are being performed to try to clarify this issue. Therefore, so far, indications are that the species turning over under realistic conditions is the same as under ultrahigh vacuum conditions.

In summary, we have presented an example where a simple reaction has been studied both under ambient and ultrahigh vacuum conditions and it is shown that the results parallel each other to a large extent so that ideas can be transferred between the two regimes. This is certainly a feature that is connected with the specific system and reaction under investigation and one has to check from system to system whether transferability is given. On the other hand, it is clear that there are cases where reaction mechanisms and structure in both regimes are the same. There is accumulating evidence that this may be the case for several systems. The example also illustrates the necessity to further develop in-situ spectroscopic techniques.

## 1.3 PROPERTIES OF INDIVIDUAL PARTICLES

The experiments reported so far, address problems of specific sites and size specific reactions and deal with samples representing ensembles of clusters with narrow size distributions. Recently, experiments have been undertaken to probe the response of individual particles using scanning probe techniques. While STS recording of current-voltage curves has been exercised for a while [65, 66], only within the last few years have deposited aggregates been investigated by probing the optical response [67, 68]. Figure 10 illustrates schematically the dipole excitation of deposited clusters. The induced dipoles in the spheres are indicated together with their image dipoles in the substrate. For the case depicted on the right, one can estimate the effect of an insulating substrate on collective electron excitations in metallic clusters [67]. Consequently, the resonance energy decreases (red shift). A scanning tunneling device can be used to induce such excitations of individual clusters and determine their optical response.

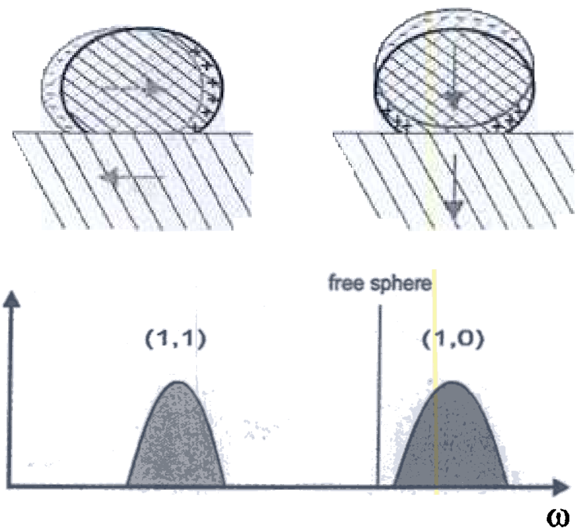

*Figure 10.* Schematic representation of the surface plasmon excitations for ellipsoids attached to a solid substrate. The modes with parallel and perpendicular excitation dipole are indicated and the resulting spectrum is schematically indicated below.

Schematically the setup is shown in Figure 11a [68, 69]. The tip is used to inject electrons into individual Ag clusters, in this case deposited on alumina for excitation. Then the light emitted from the clusters upon radiative decay is measured via a spectrometer outside the vacuum chamber [68]. Figure 11b shows the fluorescence spectra as a function of size referring to the specific clusters in the STM image, which occurs blurred because it was taken at high tunneling voltage necessary for excitation. A better representation of the size distribution of the Ag clusters is imaged in the second inset in Figure 11b although even in this case one has to take account of the fact that due to tip convolution the actual size is considerably smaller than the imaged one. The peak shows a pronounced blue shift as a function of size consistent with observations on cluster ensembles of varying size. In this context it is interesting to look at the line widths of the resonance as a function of size. This plotted in Figure 11c. The line width is smallest for the larger clusters, i.e. 0.15 eV, and increases to 0.3 eV for the smallest ones studied. We consider this to be the homogeneous line width. The fact that it changes following an inverse cluster radius reveals the influence of the cluster surface becoming more important for smaller systems as a channel to deactivate the excited state through electron-surface scattering without generating radiation.

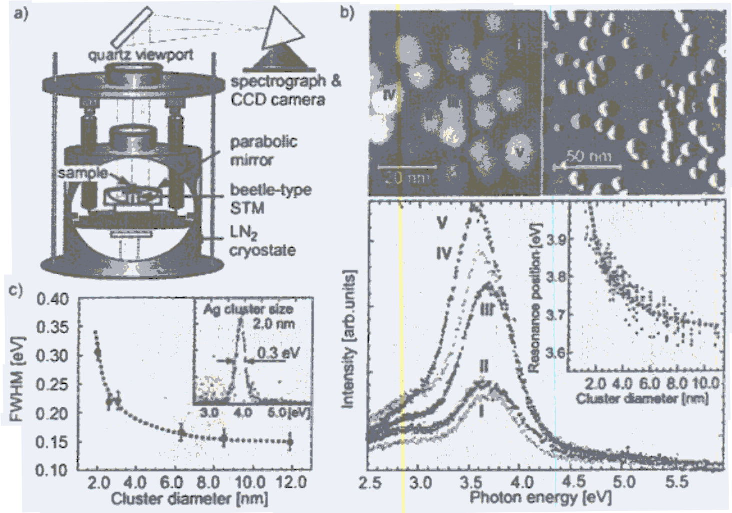

*Figure 11. a)* Schematic diagram of the experimental setup for the photon emission scanning tunneling microscope. *b)* Photon emission spectra as a function of particle size. The corresponding particles are marked in the upper left panel. The upper right panel shows a topological image of a typical cluster covered area. The size dependence of the resonance position of the plasmon excitation is shown in the inset on the left. *c)* Line widths of the observed plasmon excitation as a function of particle size.

## .4. HETEROGENIZING HOMOGENEOUS CATALYSTS

As examplified for the case of ethene hydrogenation, the application of in-situ techniques is a topic of great interest currently.

The following example represents another case where the application of in-situ techniques to model catalysts allow a detailed view at molecular processes in a reaction at surfaces [70, 71].

Transition metal (in particular titanium) halides and organoaluminum compounds have been in use since Ziegler's early work in the early 1950's [72] to (homogeneously) catalyze the polymerization of ethene [73, 74]. Together with the extension of Ziegler's work by Natta [75, 76] to use these systems in the synthesis of stereo regular poly(α)alkenes, the basis for more than 10 % of all profits made with organometallic catalysts have been laid [77]. Since the development of the first generation Ziegler-Natta catalysts, several generations of such catalysts have been put in place which exhibit orders of magnitude higher activity and efficiency [74]. The third generation of Ziegler-Natta catalysts actually represents a supported catalyst which has been developed and used since 1975 in order to increase the amount of active Ti using inorganic chlorides, such as $MgCl_2$ and $CoCl_2$ as supports [78]. The high activity of these catalysts allowed to use low catalyst concentrations and, therefore, catalyst residues can remain in the polymer [74]. The literature on the topic of Ziegler-Natta catalysis is huge and still growing since the development of the new generation of metallocenes/methylaluminoxane catalysts has recently increased interest in this field substantially [73, 79-81]. There are several excellent reviews on the subject and we would like to refer to one by W. Kaminski and M. Arndt [73], in particular.

Interesting and important contributions to our understanding have recently been gained through theoretical studies by Parrinello and his group e.g. [82].

The experimental characterization of supported third generation Ziegler-Natta catalysts has been mainly indirectly done in the past via polymer product analysis. However, knowledge on surface properties of such systems is of fundamental importance to describe the process and its mechanism in detail. Surface science studies on polymerization catalysts are rather scarce. Model studies on the Phillips catalyst have been performed [83, 84] and most importantly Somorjai and coworkers [85-90] published a series of publications on the preparation and characterization of model systems for supported Ziegler-Natta catalysts. These model systems have been used to polymerize ethene.

Following the work of Somorjai et al. [85-90] we have used a model system consisting of an epitaxially grown $MgCl_2$ film onto which $TiCl_4$ was anchored as the active component. The anchoring process has been studied by electron spectroscopy [89] and, recently in our group, by ESR spectroscopy, we have shown that surface defects in the $MgCl_2$ film are crucial in this process [71]. The key step, however, is the so-called activation of the system by adding a co-catalyst, namely an alkyl aluminum compound (trimethylaluminum (TMA), triethylaluminum (TEA)). In this process is it believed that Ti ions assume a lower oxidation state and when TMA is used radicals ($R^{\bullet}$) are created according to Equation (1), whereas the activation with TEA takes place through a disproportionation reaction [91-93].

ESR spectroscopy as another in-situ technique can be favorably used to prove the formation of radicals according to:

$$TiCl_4 + AlR_3 \rightarrow RTiCl_3 + AlClR_2 \rightarrow TiCl_3 + R^{\bullet} + AlClR_2\ (R=CH_3) \qquad (1)$$

In Figure 12 the preparation of the model system is briefly summarized. A Pd(111) substrate is covered by a $MgCl_2$ film in the (001) orientation. It grows in a layer by layer mode and the surface is terminated by chloride ions as shown by LEED and Auger spectroscopy.

Magni and Somorjai in their pioneering work already realized that it is necessary to produce defects in the film to bind the $TiCl_4$ precursor [85-91, 94]. The idea really goes back even further [95, 96], however. Early on it was noted that the uncoordinated edge and corner sites on a $MgCl_2$ crystallite bind $TiCl_4$ [78, 97] and also corroborated by recent model calculations [82, 98].

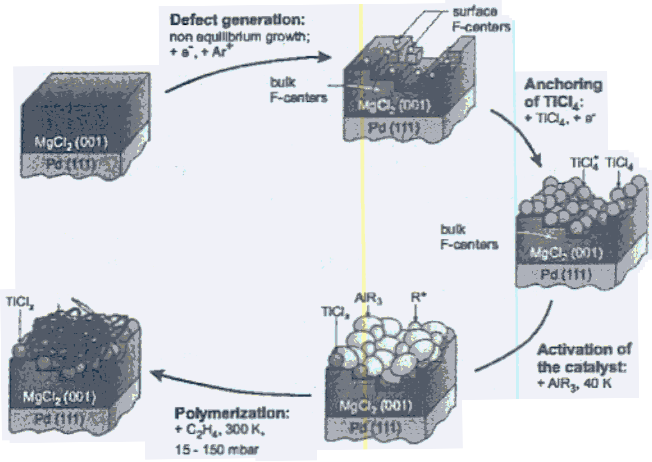

*Figure 12.* Schematic representation of the preparation of the Ziegler-Natta model catalyst.

There are several ways to produce defect containing surfaces: One way is to keep the Pd(111) surface temperature low, so that the mobility of the $MgCl_2$ is too low to produce a fully epitaxial film. However, the problem here is, that such films often contain pinholes, which change the reactivity of the system. Therefore, it has been considered to first create a fully epitaxial film and then produce defects by either electron or ion bombardment [85-91, 94]. Figure 13 compares the ESR spectra for the two cases namely defects created at lower growth temperature (bottom) and after a sequential bombardment with electrons and argon ions.

Let us first consider the non-epitaxial film. Both, position of the band in the lowest trace as well as the temperature dependence, which is Curie-like, favor the formation of color centers, i.e. removal of a Cl atom which leaves an unpaired electron behind. For a more detailed discussion of color center we resort to the work of Giamello and co-workers on color centers [99]). The position of the present signal is close to the one observed for color centers in MgO single crystals. Part of the ESR spectrum (40%) is quenched upon adsorption of $TiCl_4$ which suggests them to be located at the surface of the film.

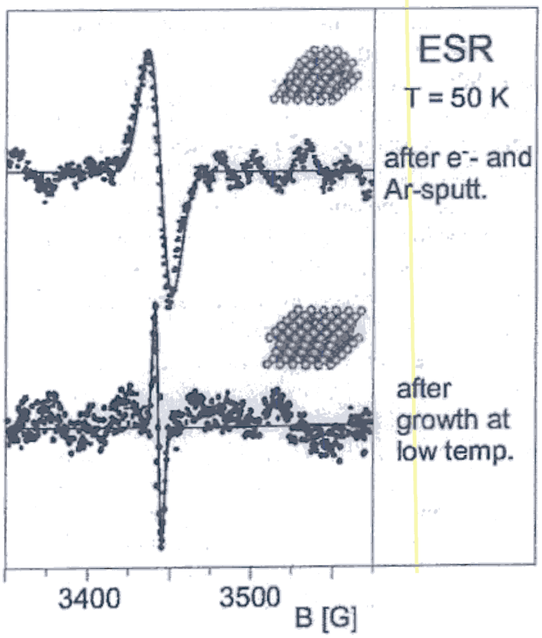

*Figure 13.* ESR spectra of color centers in a $MgCl_2$ film for two different preparation conditions. Top: An initially well-ordered film after bombardment with electrons and argon ions; Bottom: film grown at lower temperatures. Insets sketch the different environments of surface color centers for both situations.

If we grow an epitaxial film as done for the upper trace, there is no detectable ESR signal before further treatment of the film and leads to a sharp LEED pattern with low background intensity. Bombardment of the film with electrons or argon ions do disturb the structure as judged by the background of the LEED picture as well as Auger spectroscopy, which shows a loss of chlorine especially for the electron induced process. However, none of these processes alone is sufficient to create an ESR active defect. Subsequent argon ion bombardment (150 eV, 1 $\mu A/cm^2$, 3 min.) of a sample initially exposed to electrons does produce an ESR signal as shown in the upper trace Figure 13. As compared to the spectra of the defects created by growth at lower temperatures the signal is shifted to higher g-values. Additionally, the line width increases from 4 to 14 G. This might be explained by the creation of color centers on the rough surface exposing different low coordinated sites which will have slightly different g-values as compared to the color center on the (001) terrace. This geometric situation of the color centers is sketched in Figure 13.

$TiCl_4$ has a high enough vapor pressure to dose the molecule from the gas phase. Adsorption of $TiCl_4$ and subsequent electron bombardment leads to the formation of $Ti^{3+}$ centers as monitored by ESR. Depending on the preparation conditions two cases can be distinguished. For films showing the signature of paramagnetic color centers in the ESR a broad signal situated at g = 1.93 is found, whereas films without paramagnetic defects exhibit a much sharper feature centred at g = 1.96. However, there is no indication that the presence of the observed $Ti^{3+}$ signals correlates with the polymerization activity of the catalyst. The g-values found are situated among values reported for $TiCl_3$ in octahedral (g = 1.94) and tetrahedral (g = 1.97) environments [100-102]. These values have been measured for Ziegler-Natta-catalysts, but also in those cases there is no clear indication for a correlation with the catalyst activity. While the signal observed on the less defected surface is close to the value observed for tetrahedral environments the signal of the surface showing paramagnetic defects is centered at the value for octahedral environments. Comparing the line width of the signals measured here with the ones in the literature the general trend of the signal at g = 1.94 being broader than the ones at g = 1.97 holds true also for these measurements, however, the line width of the resonance at g = 1.93 is considerably broadened as compared to literature. Considering the stronger disorder of these systems it is more likely that isolated $Ti^{3+}$ centers are formed in this case which may comprise different local environments and thus showing a larger line width. The lack of an ESR signal corresponding to $Ti^{3+}$ ions in cases where no additional argon or electron bombardment has been applied, cannot be interpreted as a clear indication for the absence of $Ti^{3+}$ at the surfaces. In the literature there are discussions that small spin-lattice-relaxation times, dipole coupling and super exchange may only leave a very small fraction of $Ti^{3+}$ ESR active or detectable due to increase in line width [103, 104].

The $TiCl_4/MgCl_2$ system is, as it is called in Ziegler-Natta-catalysis, activated by exposing it to the co-catalyst, i.e. an aluminum alkyl compound. We have used trimethylaluminum (TMA) and triethylaluminum (TEA) for activation. The compounds have been dosed from the gas phase either at room temperature for a prolonged time or much shorter at 40 K surface temperature. Typically, 3400 L of TMA or TEA were exposed. The infrared spectrum of the condensed film showed the typical FTIR spectrum known from condensed and matrix isolated species [105]. There are bands that can be assigned to dimeric aluminum alkyl species.

Figure 14 shows ESR spectra after reaction of the TMA with the $TiCl_4/MgCl_2$ system [70]. A typical low coverage of $TiCl_4$ leads to the spectra shown in the upper trace. Increasing the amount of $TiCl_4$ on the surface by a factor of three increases the intensity of the ESR spectrum by a factor of 1.7, which indicates that the amount of surface titanium centers increases with total amount of titanium on the surface. This can be understood by means of an island like growth mode of the $TiCl_4$ on the surface. The spectrum is free of any $Ti^{3+}$ signal. This is in accordance with the observation in the literature namely the formation of mainly $Ti^{2+}$ species due to the reduction with aluminum alkyls [106, 107]. Although it might be thought that methyl radicals are the most natural products in the reduction of a mixed titanium-chlorine-methyl species, a comparison of the line shape of the observed spectra with spectra of methyl radicals (shown at the bottom of Figure 14) taken from the literature [108] clearly shows that the species present here are not methyl radicals. Whereas the ESR spectrum of a methyl radical is a quartet of lines the spectrum observed here, though dominated by a quartet structure, shows a couple of additional lines pointing to additional interactions of the unpaired electron. By comparing the line shape to other alkyl radicals it turned out that the present spectrum can be attributed to ethyl radicals. Figure 14 shows for comparison ethyl radicals created in an ethylchloride matrix generated by photolysis [109]. The line shape of the ethyl radicals can be understood when assuming that the protons of the methyl group adjacent to the spin containing methylene group, which cause superhyperfine interaction with the unpaired electron, are magnetically equivalent due to a fast rotation of the methyl group along the C-C bond. The two protons of the methylene group, however, give rise to anisotropic superhyperfine interaction because the adsorption of the molecule on the surface hinders a rotation of the molecule in space. Assuming the anisotropic interaction to be axially symmetric allows for a good description of the observed line shape as shown by Shiga et al. [108].

*Figure 14.* ESR spectra of alkyl radicals: *a)* after adsorption of $AlMe_3$ at 40 K on a model catalyst. Spectrum is enlarged by a factor of 2.5 as compared to b); *b)* equivalent procedure to a), for a catalyst containing a three fold higher titanium content as compared to a); *c)* ethyl radicals in an ethyl chloride matrix at 77 K [109]; *d)* methyl radicals on a silica surface at 77 K [108].

There are two key questions, that have to be answered.
1. How have the $C_2H_5$ radicals been created?
2: Have the radicals been created at the TMA/$TiCl_4$-$MgCl_2$ interface or in the TMA activating materials?

The second question can be answered by studying the amount of radicals formed as a function of the amount of $TiCl_4$ at the interface and as a function of exposed TMA. As a function of $TiCl_4$ the ESR intensity increases for a low $TiCl_4$ concentration regime but it shows a clear saturation behavior when plotted versus the amount of TMA adsorbed. Both observations are compatible with a radical creation process at the TMA-

$TiCl_4/MgCl_2$ interface, where an alkylation of the $TiCl_4$ by ligand exchange is supposed to occur. Assuming this ligand exchange to occur the primary radical that can be created is a methyl radical. For this radical there are several possibilities for consecutive reactions given the size and high mobility, even at low temperature, in the solid state [110].

The most likely reaction yielding ethyl radicals is

$$CH_3\cdot + Al(CH_3)_3 \quad \rightarrow \quad H_3C\text{-}H_2C\cdot + AlH(CH_3)_2 \qquad (2)$$

Even though such a reaction has not been investigated so far it can be crudely estimated that it is energetically possible. Above 50 K the intensity of the ethyl radicals is attenuated irreversibly and decreases below the detection limit above 80 K. This can be explained by assuming the ethyl radicals to diffuse and recombine at these temperatures, as has been observed for methyl radicals above 45 K [111] and $NO_2$ radicals on an oxide surface above 75 K [112].

After not reacted TMA has all been desorbed, still carbon due to the successful alkylation of the $TiCl_4$ is found on the surface. It is, however, important to note that after removing the reacted $TiCl_x$ moieties from the surface, e.g. by soft argon sputtering, and redosing with TMA new $C_2H_5$ radicals can be created.

An interesting observation is made if TEA is used instead of TMA. Even though the catalyst can be activated in a similar way as for TMA, radicals created from TEA have never been observed. This is in line with expectations from literature because here a disproportionation has been proposed according to:

$$AlEt_3 + TiCl_4 \rightarrow \quad AlEt_2Cl + TiCl_3Et \qquad (3)$$

$$2TiCl_3Et \quad \rightarrow \quad 2TiCl_3 + C_2H_4 + C_2H_6 \qquad (4)$$

Because ethyl radicals have been observed in the preceding experiment, which also suggest that these radicals are stable at the given temperature, the initial formation of ethyl radicals would undoubtedly lead to observation of the radicals. The absence of an ESR spectrum therefore strongly suggests a disproportionation reaction in accordance to interpretation in the literature from indirect evidence [91-93, 113].

The model catalyst was exposed to ethylene at 15 to 150 mbar, where the gas was introduced through the gas-dosing system into the IR chamber. Figure 15 shows the IR spectrum of the generated polyethylene. Characteristic are the stretching modes at 2852/2924 $cm^{-1}$, the doublets of the deformation modes at 1473/1463 $cm^{-1}$, and the rocking modes at 730/720$cm^{-1}$. In comparison with the literature the observed frequencies of the stretching modes are situated at the higher end for dominating trans-configurations. This was taken as an indication that the polymer chains have long range order in trans-configurations but also contain some gauche defects.

The course of the reaction has been studied by evaluating the IR band at 2852 $cm^{-1}$ which is the one least influenced by the presence of gaseous ethylene. The polymerization has been followed for 12 to 150 h.

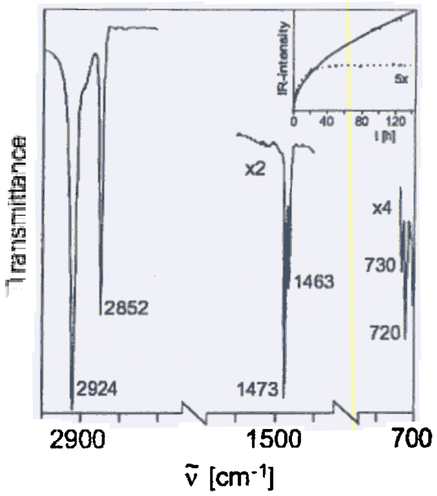

*Figure 15.* IR spectrum of polyethylene polymerized on the model catalyst. (Inset shows kinetics of the ethylene polymerization at 300 K as measured by IR spectroscopy. The full line represents the kinetics measured for a rough catalyst, the kinetics of a smooth and less defects catalyst is indicated by the dotted line).

Two different kinds of behavior have been observed. Typical results are given in the inset of Figure 15. The determining factor is here the degree of disorder in the surface of the model catalyst. While a catalyst with a high degree of disorder shows a monotonous increase of the polyethylene amount with time, catalysts prepared on a smooth and less defected surface show a self-terminating reaction after approximately 50 h leading to considerably less thick film as compared to the former case. This can be explained in a straight forward way by considering that on a smooth surface a rather smooth polymer film forms which in a relatively short time becomes impermeable for ethylene from the gas phase so that the reaction is self limiting. In the other case, the growing film possibly has a sufficient number of pores so that the monomer can continue to reach the catalyst and the reaction keeps going. This assumes that the polymerization reaction takes place at the interface of the polymer and the magnesium chloride support, which has been recently corroborated experimentally [114]. The latter behavior can be modeled by assuming that the monomer molecules are transported by diffusion to the interface. The amount of polymer $n_e$ increases with reaction time t according to

$$n_e = \delta\sqrt{t} \qquad (5)$$

where the constant δ is a function of the diffusion coefficient, the surface area, the molar volume of the polymer and the concentration at infinite time t.

Therefore, we expect that the IR intensity increases as $\sqrt{t}$ . With $\delta = 4.6 \cdot 10^{-2}$ mol $s^{-1/2}$ the fit given in Figure 15 has been obtained. In conclusion, a combination of ESR and IRAS allows us to follow the polymerisation of ethene in some detail.

## 2. Synopsis

On the basis of a variety of case studies we have reviewed the state of the art in dealing with model systems and their relation to heterogeneous catalysis. It has become clear that it is necessary to develop in-situ techniques that allow us to probe the working system. It can be foreseen that useful new and solid information on model systems under reaction conditions may be extracted that will bring closer catalysis and surface science.

## 3. References

Ertl, G., Knözinger, H. and Weitkamp, J. (eds.) (1997) *Handbook of Heterogeneous Catalysis*, Wiley-VCH Verlagsgesellschaft mbH, Weinheim, 1560.

2 Gunter, P. L. J., Niemantsverdriet, J. W. H., Ribeiro, F. H. and Somorjai, G. A. (1997) *Catal. Rev. Sci. Eng.* **39**, 77.

3. Henry, C. R. (1998) *Surf. Sci. Rep.* **31**, 231.

4. Campbell, C. T. (1997) *Surf. Sci. Rep.* **27**, 1.

5. Goodman, D. W. (1995) *Surf. Rev. Lett.* **2**, 9.

6. Diebold, U., Pan, J.-M. and Madey, T. E. (1995) *Surf. Sci.* **331-333**, 845.

7. Freund, H.-J. (1997) *Angew. Chem. Int. Ed. Engl.* **36**, 452.

8. Freund, H.-J. (2002) *Surf. Sci.* **500**, 271.

9. Freund, H.-J., Bäumer, M. and Kuhlenbeck, H. (2000) *Adv. Catal.* **45**, 333.

10. Heiz, U., Vanolli, F., Trento, L. and Schneider, W. D. (1997) *Rev. Sci. Instrum.* **68**, 1986.

11. Freund, H.-J. (1995) *Phys. Status Solidi b* **192**, 407.

12. Jaeger, R. M., Kuhlenbeck, H., Freund, H.-J., Wuttig, M., Hoffmann, W., Franchy, R. and Ibach, H. (1991) *Surf. Sci.* **259**, 235.

13. Libuda, J., Winkelmann, F., Bäumer, M., Freund, H.-J., Bertrams, T., Neddermeyer, H. and Müller, K. (1994) *Surf. Sci.* **318**, 61.

14. Gassmann, P., Franchy, R. and Ibach, H. (1994) *Surf. Sci* **319**, 95.

15. Franchy, R., Masuch, J. and Gassmann, P. (1996) *Appl. Surf. Sci.* **93**, 317.

16. Bardi, U., Atrei, A. and Rovida, G. (1992) *Surf. Sci.* **268**, 87.

17 Becker, C., Kandler, J., Raaf, H., Linke, R., Pelster, T., Dräger, M., Tanemura, M. and Wandelt, K. (1998) *J. Vac. Sci. Technol. A* **16**, 1000.

Graupner, H., Hammer, L., Heinz, K. and Zehner, D. M. (1997) *Surf. Sci.* **380**, 335.

19. Uebing, C. (1998) *Ber. Bunsenges. Phys. Chem.* **102**, 1156.

20. Bäumer, M. and Freund, H.-J. (1999) *Progr. Surf. Sci.* **61**, 127.

21. Libuda, J., Frank, M., Sandell, A., Andersson, S., Brühwiler, P. A., Bäumer, M., Mårtensson, N. and Freund, H.-J. (1997) *Surf. Sci.* **384**, 106.
22. Heemeier, M., Frank, M., Libuda, J., Wolter, K., Kuhlenbeck, H., Bäumer, M. and Freund, H.-J. (2000) *Catal. Lett.* **68**, 19.
23. Stempel, S., Bäumer, M. and Freund, H.-J. (1998) *Surf. Sci.* **402-404**, 424.
24. Frank, M. and Bäumer, M. (2000) *Phys. Chem. Chem. Phys.* **2**, 3723
25. Heemeier, M., PhD thesis, Freie Universität Berlin (in preparation).
26. Heemeier, M., Stempel, S., Shaikhutdinov, S., Libuda, J., Bäumer, M., Oldman, R. J., Jackson, S. D. and Freund, H.-J. (in press) *Surf. Sci.*
27. Hansen, K. H., Worren, T., Stempel, S., Lægsgaard, E., Bäumer, M., Freund, H.-J., Besenbacher, F. and Stensgaard, I. (1999) *Phys. Rev. Lett.* **83**, 4120.
28. Ernst, N., Duncombe, B., Bozdech, G., Naschitzki, M. and Freund, H.-J. (1999) *Ultramicroscopy* **79**, 231.
29. Piednoir, A., Perrot, E., Granjeaud, S., Humbert, A., Chapon, C. and Henry, C. R. (1997) *Surf. Sci.* **391**, 19.
30. Unterhalt, H., Rupprechter, G. and Freund, H.-J. (2002) *J. Phys. Chem.* **B106**, 356.
31. Sinfelt, J. H. (1983) *Bimetallic Catalysts*, Wiley, New York.
32. Idriss, H., Diagne, C., Hindermann, J. P., Kinnemann, A. and Barteau, M. A., 10th International Congress on Catalysis (eds. Guczi, L., Solymosi, F. and Tetenyi, P.), Budapest, Elsevier (1992).
33. Kapoor, M. P., Lapidus, A. L. and Krylova, A. Y., 10th International Congress on Catalysis (eds. Guczi, L., Solymosi, F. and Tetenyi, P.), Budapest, Elsevier (1992) 2741.
34. Juszczyk, W., Karpinski, Z., Lomot, D., Pielaszek, J., Paal, Z. and Stakheev, A. Y. (1993) *J. Catal.* **142**, 617.
35. Noronha, F. B., Schmal, M., Nicot, C., Moraweck, B. and Frety, R. (1997) *J. Catal.* **168**, 42.
36. Bischoff, S., Weight, A., Fujimoto, K. and Lucke, B. (1995) *J. Mol. Catal.* **95**, 259.
37. Weissermel, K. and Arpe, H.-J. (1997) *Industrial Organic Chemistry*, VCH Weinheim, Weinheim, Germany.
38. Gimenez, F., Chapon, C. and Henry, C. R. (1998) *New Journal of Chemistry* **22**, 1289.
39. Giorgi, J., Chapon, C. and Henry, C. R. (1999) in Braunstein, P., Oro, L. A. and Raithby, P. R. (eds.), *Metal Clusters in Chemistry*, Wiley, Weinheim, pp. 1194.
40. Hill, T., Mozaffari-Afshar, M., Schmidt, J., Risse, T., Stempel, S., Heemeier, M. and Freund, H.-J. (1998) *Chem. Phys. Lett.* **292**, 524.
41. Bäumer, M., Frank, M., Heemeier, M., Kühnemuth, R., Stempel, S. and Freund, H.-J. (2000) *Surface Science* **454**, 957.
42. M. Heemeier, Carlsson, A. F., M., Naschitzki, M., Schmal, M., Bäumer, M. and Freund, H.-J. (2002) *Angew. Chem., Intern. Ed.* **in press**,
43. Schauermann, S., Hoffmann, J., Johanek, V., Hartmann, J., Libuda, J. and Freund, H.-J. (2002) *Angew. Chem. Int. Ed.* **41**, 2532.
44. Kok, G. A., Noordermeer, A. and Nieuwenhuys, B. E. (1983) *Surf. Sci.* **135**, 65.
45. Holroyd, R. P. and Bowker, M. (1997) *Surf. Sci.* **377-379**, 786.

46. Rebholz, M. and Kruse, N. (1991) *J. Chem. Phys.* **95**, 7745.
47. Chen, J.-J., Jiang, Z.-C., Zhou, Y., Chakraborty, B. R. and Winograd, N. (1995) *Surf. Sci.* **328**, 248.
48. Libuda, J., Meusel, I., Hartmann, J. and Freund, H.-J. (2000) *Rev. Sci. Instrum.* **71**, 4395.
49. Meusel, I., Hoffmann, J., Hartmann, J., Heemeier, M., Bäumer, M., Libuda, J. and Freund, H.-J. (2001) *Catal. Lett.* **71**, 5.
50. Wolter, K., Seiferth, O., Kuhlenbeck, H., Bäumer, M. and Freund, H.-J. (1998) *Surf. Sci.* **399**, 190.
51. Hoffmann, F. M. (1983) *Surf. Sci. Rep.* 3, 107.
52. Hollins, P. (1992) *Surf. Sci. Rep.* **16**, 51.
53. Shaikhutdinov, S. K., Heemeier, M., Bäumer, M., Lear, T., Lennon, D., Oldman, R. J., Jackson, S. D. and Freund, H.-J. (2001) *J. Catal.* **200**, 330.
54. Frank, M., Bäumer, M., Kühnemuth, R. and Freund, H.-J. (2001) *J. Vac. Sci. Technol.* **A19**, 1497.
55. Christmann, K. (1988) in Paal, Z. and Menon, P. G. (eds.), *Hydrogen Effects in Catalysis*, Dekker, New York, pp. 3.
56. Godbey, D., Zaera, F., Yeates, R. and Somorjai, G. A. (1986) *Surf. Sci.* **167**, 150.
57. Sekitani, T., Takaoka, T., Fujisawa, M. and Nishijima, M. (1992) *J. Phys. Chem.* **96**, 8462.
58. Somorjai, G. A. (1994) *Introduction to Surface Chemistry and Catalysis*, John Wiley & Sons, Inc., New York.
59. Shaikhutdinov, S., Frank, M., Bäumer, M., Jackson, S. D., Oldman, R. J., Hemminger, J. C. and Freund, H.-J. (2002) *Catal. Lett.* **80**, 125.
60. Rupprechter, G., Unterhalt, H., Morkel, M., Galletto, P., Hu, L. and Freund, H.-J. (2002) *Surf. Sci.* **502-503**, 109.
61. Rupprechter, G. (2001) *Phys. Chem. Chem. Phys.* **3**, 4621.
62. Dellwig, T., Rupprechter, G., Unterhalt, H. and Freund, H.-J. (2000) *Phys. Rev. Lett.* **85**, 776.
63. Rupprechter, G., Unterhalt, H., Hu, L. and Freund, H.-J. (in preparation) *J. Catal.*
64. Rupprechter, G., Dellwig, T., Unterhalt, H. and Freund, H.-J. (2001) *Topics in Catalysis* **15**, 19.
65. Rainer, D. R. and Goodman, D. W. (1997) in Lambert, R. M. and Pacchioni, G. (eds.), *Chemisorption and Reactivity on Supported Clusters and Thin Films*, Kluwer, Dordrecht, pp. 27.
66. Valden, M., Lai, X. and Goodman, D. W. (1998) *Science* **281**, 1647.
67. Kreibig, U. and Vollmer, M. (1995) *Optical Properties of Metal Clusters*, Springer, Berlin, 1-532.
68. Nilius, N., Ernst, N. and Freund, H.-J. (2000) *Phys. Rev. Lett.* **84**, 3994.
69. Coombs, J. H., Gimzewski, J. K., Reihl, B., Sass, J. K. and Schlittler, R. R. (1988) *J. Microscopy* **152**, 325.
70. Risse, T., Schmidt, J., Hamann, H. and Freund, H.-J. (2002) *Angew. Chem. Int. Ed. Engl.* **41**, 1518.
71 Schmidt, J., Risse, T., Hamann, H. and Freund, H.-J. (2002) *J. Chem. Phys.* **116**, 10861.

72. Ziegler, K., Holzkamp, E., Martin, H. and Breil, H. (1955) *Angew. Chem.* **67**, 541.
73. Barbé, P. C., Cecchin, G. and Noristi, L. (1987) *Adv. Polym. Sci.* **81**, 1.
74. Kaminsky, W. and Arndt, M. (1997) Ziegler-Natta Polymerization, in G. Ertl, H. Knözinger and Weitkamp, J. (eds.), *Handbook of Heterogeneous Catalysis*, Wiley-VCH, Weinheim, pp. 2405.
75. Natta, G. (1955) *J. Polym. Sci.* **16**, 143.
76. Natta, G., Pino, P. and Mazzanti, P., U.S.-Patent to Montedison Ital. Priority (1954).
77. Fink, G., Mühlhaupt, R. and Brintzinger, H. H. (eds.) (1994) *Ziegler Catalysts*, Springer-Verlag, Heidelberg.
78. Dusseault, J. J. A. and Hsu, C. C. (1993) *J. Macromol. Sci. - Rev. Macromol. Chem. Phys.* **C 33**, 103.
79. Mason, M. R. (1993) *J. Am. Chem. Soc.* **115**, 4971.
80. Harlan, C. J., Mason, M. R. and Barron, A. R. (1994) *Organometallics* **13**, 2957.
81. Sinn, H. (1995) *Macromol. Symp.* **97**, 27.
82. Boero, M., Parrinello, M., Weiss, H. and Hüfter, S. (2001) *J. Phys. Chem. A* **105**, 5096.
83. Hemmerich, I., Rohr, F., Seiferth, O., Dillmann, B. and Freund, H.-J. (1997) *Z. Phys. Chem.* **202**, 31.
84. Thüne, P. C., Loos, J., Lemstra, P. J. and Niemantsverdriet, H. (1999) *J. Catal.* **183**, 1.
85. Magni, E. and Somorjai, G. A. (1995) *Appl. Surf. Sci.* **89**, 187.
86. Magni, E. and Somorjai, G. A. (1995) *Catal. Lett.* **35**, 205.
87. Magni, E. and Somorjai, G. A. (1996) *Surf. Sci.* **345**, 1.
88. Magni, E. and Somorjai, G. A. (1996) *J. Phys. Chem.* **100**, 14786.
89. Korányi, T. A., Magni, E. and Somorjai, G. A. (1999) *Topics in Catalysis* **7**, 179.
90. Kim, S. H. and Somorjai, G. A. (2000) *Appl. Surf. Sci.* **161**, 333.
91. Thewalt, U. (1977) Titan-Organische Verbindungen, in *Gmelins Handbuch der Anorganischen Chemie*, Springer Verlag, Heidelberg.
92. de Vries, H. (1961) *Rec. Trav. Chim.* **80**, 866.
93. Beermann, C. and Bestian, H. (1959) *Angew. Chem.* **71**, 618.
94. Magni, E. and Somorjai, G. A. (1995) *Surf. Sci. Lett.* **341**, L 1078.
95. Galli, P., Barbé, P. C., Guidetti, G., Zannetti, R., Marigo, A., Bergozza, M. and Fichera, A. (1983) *Eur. Polym. J.* **19**, 19.
96. Gerbasi, R., Marigo, A., Martorana, A., Zannetti, R., Guidetti, G. and Baruzzi, G. (1984) *Eur. Polym. J.* **20**, 967.
97. Corradini, P. and Guerra, G. (1991) *Polym. Sci.* **16**, 239.
98. Martinsky, C., Minot, C. and Ricart, J. M. (2001) *Surf. Sci.* **490**, 237.
99. Giamello, E., Murphy, D., Ravera, L., Coluccia, S. and Zecchina, A. (1994) *J. Chem. Soc. Faraday Trans.* **90 (20)**, 3167.
100. Peyroche, J., Girard, Y., Laputte, R. and Guyot, A. (1969) *Makromol. Chem.* **129**, 215.
101. Soga, K. and Terano, M. (1981) *Makromol. Chem.* **182**, 2439.
102. Zakharov, V. A., Makhtarulin, S. I., Poluboyraov, V. A. and Anufrienko, V. F. (1984) *Makromol. Chem.* **185**, 1781.

103. Chien, J. C. W. and Wu, J. C. (1982) *J. Polym. Sci., Polym. Chem. Ed.* **20**, 2461.
104. Fuhrmann, H. and Herrmann, W. (1994) *Macromol. Chem. Phys.* **195**, 3509.
105. Kvisle, S. and Rytter, E. (1984) *Spectrochim. Acta* **40 (10)**, 939.
106. Magni, E. and Somorjai, G. A. (1997) *Surf. Sci.* **377-379**, 824.
107. Kim, S. H. and Somorjai, G. A. (2001) *J. Phys. Chem. B* **105**, 3922.
108. Shiga, T., Yamaohu, H. and Lund, A. (1974) *Z. Naturforsch. A* **29**, 653.
109. Ayscough, P. B. and Thomson, C. (1962) *Trans. Faraday Soc.* **58**, 1477.
110. Morehouse, R. L., Christiansen, J. J. and Gordy, W. (1966) *J. Chem. Phys.* **45 (5)**, 1751.
111. Toriyama, K., Iwasaki, M. and Nunome, K. (1979) *J. Chem Phys.* **71 (4)**, 1968.
112. Schlienz, H., Beckendorf, M., Katter, U. J., Risse, T. and Freund, H.-J. (1995) *Phys. Rev. Lett.* **74**, 761.
113. D'yachowvskii, F. S., Khrushch, N. E. and Shilov, A. E. (1968) *Kin. Catal. (USSR)* **9**, 831.
114. Kim, S. H. and Somorjai, G. A. (2000) *Catal. Lett.* **68**, 7.